mathematics

MDPI

Article

Differential Geometric Signatures of Persistent Structural Transitions in Solar Wind Dynamic Pressure via Bézier Representations

Emre Eroglu

Department of Mathematics, Faculty of Arts and Sciences, Kirklareli University, Kirklareli 39100, Türkiye; eroglumre@gmail.com

Abstract

Traditional time-domain signal analysis typically characterizes a signal directly in its original domain, potentially overlooking structural information encoded in its geometry. This study proposes a geometric-algebraic framework for characterizing transient and persistent transitions in solar wind dynamic pressure. The dynamic pressure is a fundamental parameter describing the momentum flux of the solar wind and its mechanical forcing on the terrestrial magnetosphere. The analysis begins by representing the time-domain observations as points (t_i, P_i), $i = 0, 1, 2, \ldots$ followed by segmentation and parametric *Bézier* curve representation using quadratic, cubic, and quartic polynomial forms. Differential geometric and algebraic quantities derived from these representations are combined into a multidimensional *signature*. Rather than assigning anomalous labels directly to individual observations, empirical reference structures are constructed from normal and anomalous signal segments, while the investigated observations remain blind during reference construction. Their relative distances to the normal and anomalous reference manifolds are then evaluated using a degree-consensus strategy to assess the persistence of directional transitions across polynomial representations. The final rolling sequence exhibits a coherent transition from consecutive normal-directed states to consecutive anomalous-directed states, with the final window showing positive consensus across all investigated polynomial degrees. The resulting signature therefore characterizes the transition as a persistent geometric movement toward the anomalous reference structure rather than merely as a pointwise amplitude anomaly. The framework provides an alternative geometric-algebraic representation of solar wind dynamic pressure variability and establishes a basis for its application to related solar wind and space weather parameters.

Keywords: Bézier curve; differential geometry; geometric transition detection; solar wind dynamic pressure; geometric feature space

MSC: 53Z05; 85-10; 85A35

Check for updates

Academic Editor: Jay M. Jahangiri

Received: 27 August 2026
Revised: 11 October 2026
Accepted: 15 October 2026
Published: 3 November 2026

Copyright: © 2026 by the author. Licensee MDPI, Basel, Switzerland. This article is an open access article distributed under the terms and conditions of the Creative Commons Attribution (CC BY) license.

1. Introduction

The solar wind plasma is continuously coupled to the near-Earth space environment and constitutes one of the major external drivers of variability in the coupled solar wind–magnetosphere–ionosphere [1,2] system. The dynamic pressure is among the fundamental solar wind parameters because it characterizes the momentum flux of the plasma flow and contributes directly to the compression and expansion of the terrestrial magnetosphere. Consequently, temporal fluctuations in the dynamic pressure may contain information

about changes in the interplanetary environment and about the response of the coupled solar wind–magnetosphere system [3].

Oscillations in the pressure have been investigated in the context of pressure pulses, sudden impulses, shock-related compressions, magnetospheric compression, and other solar wind-driven disturbances. Rapid increases in dynamic pressure can compress the magnetosphere and can contribute to identifiable responses in geospace observations, including geomagnetic sudden commencements and other magnetospheric and ionospheric responses [4]. However, the physical interpretation of an individual pressure enhancement generally requires simultaneous consideration of other solar wind and geomagnetic parameters. In particular, a pressure enhancement alone does not uniquely identify the interplanetary origin or physical structure responsible for the disturbance, since different solar wind structures can produce comparable variations in dynamic pressure [4]. Therefore, a useful characterization framework should distinguish the mathematical identification of a structural change in the time-domain signal from the subsequent physical interpretation of its origin.

Time series methods provide a natural framework for describing temporal variations in solar wind parameters. Conventional approaches, however, generally operate directly on the scalar sequence and characterize changes in terms of amplitudes, thresholds, statistical deviations, spectral properties, or related time-domain descriptors. Such representations are highly useful for identifying variability and disturbances, but they do not necessarily provide an explicit description of how the local structural organization of a signal evolves geometrically with time. Two time-dependent signals may exhibit comparable amplitude variations while possessing substantially different local curvature, gradient structure, or higher-order geometric organization. This motivates consideration of an alternative representation in which a temporal signal is treated not only as a sequence of scalar observations but also as a geometric and algebraic object.

Parametric curve representations provide a natural connection between time series data and differential geometry. Once a temporal signal is represented as a parametric curve, quantities related to derivatives, gradients, curvature, and other geometric descriptors can be evaluated along the representation. Bézier [5] curves are particularly attractive in this context because they provide polynomial parametric representations whose geometry is directly controlled by a finite set of control points [6,7]. Different polynomial degrees can consequently provide complementary representations of the same temporal structure and can be used to examine whether an observed geometric characteristic depends strongly on a particular polynomial representation. The use of a family of polynomial representations therefore provides an additional level of structural consistency beyond the interpretation of a single fitted curve.

The central hypothesis of this study is that physically contextualized structural changes in a solar wind time series may leave persistent signatures in an alternative geometric representation. Under this hypothesis, an anomalous transition should not be characterized solely by the amplitude of an individual observation. Instead, it can be characterized through the movement of consecutive temporal windows within a multidimensional geometric feature space relative to reference structures representing normal and anomalous signal behavior. Such a formulation shifts the focus from pointwise anomaly labeling toward the persistence and directionality of structural evolution.

To investigate this hypothesis, observations of solar wind dynamic pressure are first represented as points in the time–pressure plane, (t_i, P_i), $i = 0, 1, 2, \ldots$, and subsequently represented by a family of parametric Bézier curves [8]. Quadratic [9], cubic [10,11], and quartic polynomial Bézier representations are considered to examine the consistency of the extracted structural information across polynomial degrees. Differential geometric

quantities and complementary structural descriptors derived from these representations are combined into a multidimensional geometric signature. Empirical reference structures are then constructed from normal and anomalous reference observations. Importantly, the investigated observations are kept blind during the construction of these reference structures. Their subsequent positions are evaluated independently through their geometric distances from the normal and anomalous reference manifolds.

A further objective is to determine whether the extracted movement toward the anomalous reference structure persists across neighboring temporal windows and across different polynomial representations. For this purpose, a degree-consensus strategy is introduced. Positive manifold scores are interpreted as relative movement toward the anomalous reference structure, whereas negative scores indicate relative movement toward the normal reference structure. This directional information is deliberately distinguished from manifold membership: movement toward an anomalous reference manifold does not, by itself, imply that an observation has entered or belongs to that manifold. The resulting framework is therefore not intended to replace conventional physical, statistical, or time series analyses of solar wind observations. Rather, it provides a complementary representation through which temporal evolution can be examined as a persistent structural transition in a geometric-algebraic space.

The principal objective of the study is therefore to understand whether persistent transitions in dynamic pressure behavior can be identified through a Bézier-based differential geometric [12,13] representation and whether these transitions remain directionally consistent across alternative polynomial representations. The approach is initially developed for dynamic pressure because its physical interpretation and role in solar wind–magnetosphere coupling are comparatively well established [14]. The same mathematical framework may subsequently be extended to related solar wind parameters, such as proton density, and ultimately to more complex geophysical observations such as total electron content. The present study thus constitutes an initial application of a broader geometric-algebraic methodology for characterizing persistent structural transitions in geophysical time series.

2. Data

This part discusses the *dynamic pressure* [15] and related data with three different sets. The dynamic pressure P (nPa) represents the momentum flux carried by the solar wind plasma and is approximately proportional to the proton density and the square of the bulk solar wind speed. Variations and sudden enhancements in dynamic pressure can modify the pressure balance at the terrestrial magnetopause and produce magnetospheric compression and associated geospace responses. However, dynamic pressure variations alone do not uniquely determine the physical origin or geoeffectiveness of a solar wind disturbance.

The dynamic pressure used in the discussion is a dataset obtained from OMNIWeb [16], with hourly resolution and units in nPa. Set N is a low-variability reference dataset. Set N comprises 101 dynamic pressure observations, expressed in nPa, selected from the period between 28 December 2024 and 5 January 2025. The observations are selected to represent comparatively regular pressure behavior, characterized by limited abrupt fluctuations and relatively small amplitude variations. The first two observations are 2.73 and 2.23 nPa, recorded at 00:00 and 01:00 UT on 28 December 2024, respectively, whereas the final two observations are 1.42 and 1.57 nPa, recorded at 01:00 and 02:00 UT on 5 January 2025. The designation *normal* refers exclusively to the relatively stable morphological characteristics of this reference dataset. It does not imply statistical normality or classification according to an independently established quiet space weather criterion. As summarized in Table 1, dynamic pressure values range from 1.05 to 3.01 nPa, with a standard deviation of approximately 0.43 nPa, representing the lowest dispersion among the three datasets.

Table 1. Descriptive analysis.

Dataset	Number	Minimum	Maximum	Mean	Median	Standard Deviation
Normal	101	1.05	3.01	1.870495	1.88	0.429293
Anomalous	101	1.66	32.11	8.729901	7.45	6.148294
Mixed (Blind)	101	0.94	13.37	3.310792	2.54	2.192486

Set A is a high-variability reference dataset. Set A consists of 101 dynamic pressure observations selected from the period between 31 December 2024 and 13 November 2025. Unlike Set N, these observations are selected to represent pronounced short-term fluctuations, abrupt increases and decreases, and substantial amplitude variability. The first two observations are 1.66 and 7.81 nPa, recorded at 16:00 and 17:00 UT on 31 December 2024, respectively, while the final observation is 24.98 nPa, recorded at 14:00 UT on 13 November 2025. Importantly, set A does not constitute a continuous record of a single solar wind event. The term *anomalous* is used as an operational reference designation describing a comparatively complex and highly variable pressure morphology. It does not necessarily indicate statistical outliers or establish an association with a particular coronal mass ejection (CME) or interplanetary coronal mass ejection (ICME). Dynamic pressure values range from 1.66 to 32.11 nPa, with a standard deviation of approximately 6.15 nPa, indicating the greatest dispersion among the three datasets.

Set M is an independent continuous mixed and *blind* dataset. Set M comprises 101 consecutive hourly dynamic pressure observations extending from 22:00 UT on 5 May 2023 to 02:00 UT on 10 May 2023. Unlike the reference datasets, this sequence is retained without morphology-based preselection or filtering. The first two observations are 1.30 and 1.13 nPa, whereas the final two observations are 5.72 and 4.36 nPa. The continuous temporal structure of Set M preserves the natural evolution of dynamic pressure, allowing relatively stable and highly variable behavior to occur within the same observational sequence. Accordingly, Set M serves as an independent blind dataset for evaluating the response of the proposed Bézier-based geometric framework to different local pressure morphologies. Its observations are excluded from reference construction and parameter determination.

As reported in Table 1, Set M exhibits dynamic pressure values between 0.94 and 13.37 nPa, with a mean of approximately 3.31 nPa and a standard deviation of approximately 2.19 nPa.

One may see their common analytical structure and temporal interpretation. All three datasets contain 101 observations and are processed using a common observation-index structure. However, the interpretation of this index differs between the reference and blind datasets. For Sets N and A, the index denotes the ordered sequence of selected observations and does not necessarily represent consecutive physical hours. For Set M, consecutive indices correspond directly to consecutive hourly measurements. The normal and anomalous reference datasets are intentionally constructed to represent contrasting levels of dynamic pressure variability. Their selection is based primarily on the morphological characteristics of the observations rather than on mutually exclusive calendar intervals or independently verified physical event labels. Consequently, temporal overlap between the source periods, and potential overlap between individual observations, cannot be excluded. The resulting reference structures should therefore be interpreted as empirical representations of relatively low- and high-variability pressure behavior, rather than as statistically independent or physically exclusive populations.

Although the source periods of Sets N and A overlap near the end of December 2024, the datasets are defined by their respective selection criteria and morphological characteristics rather than by mutually exclusive calendar intervals. The distinction between

observation order and elapsed physical time is retained when interpreting the resulting geometric signatures.

The same segmentation scheme, Bézier polynomial degrees, and geometric comparison procedures are applied to all three datasets. This common analytical structure enables the investigation of morphological differences under consistent computational conditions while preserving the distinction between selected reference sequences and the continuous blind record.

Quadratic, cubic, and quartic order piece-wise Bézier curves govern the segmentation of datasets. The piecewise continuity of the datasets is managed with six-observation shared-endpoint segmentation and eight-hour rolling window analysis. The six-observation shared-endpoint segmentation generates a C^0 continuous piecewise Bézier representation across the entire curve, while the eight-hour rolling segmentation provides an overlapping sampling pattern to track the temporal evolution of the derived geometric signature. The eight-observation rolling window is presented with windows of 0–7, 1–8, 2–9, …, 92–99, 93–100 h. The eight-observation window length is adopted as a fixed operational scale for local geometric characterization. This length provides sufficient within-window information for constructing the degree-2, degree-3, and degree-4 Bézier representations and their associated differential geometric descriptors, while remaining short enough to preserve the temporal localization of structural changes. The one-observation stride produces strongly overlapping consecutive windows, allowing the evolution of the geometric signature to be followed progressively rather than through disjoint temporal blocks. Accordingly, the eight-observation window should be regarded as a predefined analysis scale rather than an optimized or physically unique timescale.

Table 1 shows the interval of the values of the sets.

3. Theoretical Background

3.1. Time-Domain Representation of Solar Wind Dynamic Pressure

Suppose that the observed dynamic pressure signal is represented by a sequence of ordered observations

$$\mathcal{D} = \{(t_i, P_i)\}_{i=0}^{N-1} \tag{1}$$

where t_i denotes the temporal coordinate, and P_i denotes the corresponding dynamic pressure (nPa).

The original observations are initially retained in their time-domain form. Thus, no anomalous interpretation is assigned at the level of individual observations. Instead, the signal is considered as a discrete geometric object embedded in the time-pressure plane. This representation provides the basis for constructing local parametric approximations while preserving the temporal ordering of the observations.

The principal objective is not to replace the physical interpretation of the dynamic pressure signal, but to investigate whether persistent structural transitions can be detected through an alternative geometric representation.

3.2. Segmentation and Parametric Bézier Representation

To investigate the local geometric organization of the signal, the time-domain observations are divided into consecutive segments. For each segment, a parametric polynomial Bézier representation is constructed.

Definition 1. *For a Bézier curve of degree d, the parametric representation is written as*

$$\mathbf{B}_d(u) = \sum_{j=0}^{d} \binom{d}{j} (1-u)^{d-j} u^j \mathbf{Q}_j;\ 0 \le u \le 1 \tag{2}$$

where $\mathbf{Q}_j$ *denotes the j-th control point and* $B_{j,d}(u)$ *denotes the corresponding Bernstein basis polynomial [17].*

The present analysis considers quadratic, cubic, and quartic representations. Consequently, the same temporal segment is described through three polynomial representations of different degrees. This degree family is used deliberately to reduce dependence on a single polynomial representation and to investigate whether the resulting structural signature remains consistent under alternative local geometric descriptions.

For the piecewise Bézier representation used to visualize the pressure signals, each segment is parameterized by $u \in [0,1]$, with its temporal coordinate prescribed as $x(u) = t_0 + (t_1 - t_0)u$. The pressure component is expressed in the Bernstein basis as $y_d(u) = \sum_{j=0}^{d} B_{j,d}(u) P_j^y$, where $d \in \{2,3,4\}$. The first and last pressure control coordinates are fixed at the observed segment endpoints, while the intermediate pressure control coordinates are determined by least-squares minimization. Thus, only the pressure coordinates are optimized; the temporal component is not freely fitted. The resulting curve is a constrained parametric Bézier representation that can equivalently be expressed as a polynomial graph $y = f(x)$, since the temporal component is affine and invertible. Adjacent segments share their observed boundary points, ensuring C^0 continuity.

For the published piecewise fitting experiment, the 101 observations are divided into 20 segments with shared endpoints, indexed 0–5, 5–10, …, 95–100. This construction is distinguished from the eight-observation rolling-window analysis used for extracting geometric signatures.

3.3. Differential Geometric Characterization

Once a parametric Bézier representation is obtained, differential geometric quantities are calculated along each segment.

Definition 2. *For a planar parametric curve*

$$\mathbf{B}(u) = (x(u), y(u)) \tag{3}$$

its first and second derivatives provide local information about the evolution of the curve. In particular, the derivative structure permits the calculation of quantities related to local gradient and curvature [13].

In the rolling-window geometric analysis, each eight-observation window is independently approximated by a degree-(d) polynomial fitted against normalized local time using least squares. The fitted polynomial is evaluated through its first and second-order derivatives to construct the local geometric descriptors. Since a polynomial graph admits an equivalent Bernstein–Bézier representation of the same degree, the polynomial and Bézier descriptions are mathematically compatible at the representation level. Nevertheless, the rolling-window polynomial fits are not subject to the fixed-endpoint constraints imposed in the piecewise Bézier visualization. The two fitting procedures are therefore distinguished explicitly.

Definition 3. *The curvature* $(\kappa(u))$ *is represented in the usual planar form,*

$$\kappa(u) = \frac{|x'(u)y''(u) - x''(u)y'(u)|}{\left[x'(u)^2 + y'(u)^2\right]^{3/2}} \tag{4}$$

where defined.

In addition to curvature-related quantities, derivative-based and polynomial-geometric quantities are calculated from the fitted representation. These quantities are subsequently summarized over each local segment to construct a multidimensional geometric signature.

The purpose of this stage is not to assign a physical cause to a local geometric variation. Rather, the extracted quantities provide structural descriptors through which different temporal portions of the signal can be compared in an alternative geometric space.

3.4. Five-Dimensional Geometric Signature

Definition 4. *For each rolling window, the extracted geometric information is reduced to a five-dimensional signature,*

$$\mathbf{S} = (K, G, D, L_2, C_{KG}) \tag{5}$$

where the individual components characterize different aspects of the local geometric organization. The five descriptors are not selected as previously established physical indices. They are constructed to provide complementary information on distinct aspects of the local curve geometry: curvature redistribution (K), first-order variation represented through the gradient-related descriptor (G), second-order implicit structure through the bordered Hessian descriptor (D), spectral redistribution of the associated geometric matrix (L_2), and coupling between curvature and gradient (C_{KG}). The purpose of combining these quantities is therefore to obtain a compact but heterogeneous geometric representation rather than to optimize a predefined classifier. No blind-set information is used in selecting or fitting these descriptors.

The five descriptors are constructed to represent complementary mathematical aspects of the local geometric structure; they are not assumed to be statistically independent. Because they are derived from the same fitted representation, correlations among individual descriptors may occur. The proposed signature therefore aims at geometric complementarity rather than empirical independence or statistical orthogonality.

The first component, K, represents the dynamic range of the curvature-related quantity. The second component, G, represents the corresponding dynamic range of the gradient-related quantity. The third component, D, characterizes the redistribution of the bordered Hessian determinant relative to its mean magnitude. The fourth component, L_2, represents the dynamic range of the second eigenvalue of the associated geometric matrix. The fifth component, C_{KG}, represents the correlation between curvature and gradient.

Definition 5. *For quantities z for which a ratio-based descriptor (R_z) is used, the corresponding feature is calculated from the maximum-to-minimum behavior,*

$$R_z = \frac{\max(z)}{\min(z) + \varepsilon} \tag{6}$$

with appropriate numerical stabilization where necessary.

Definition 6. *The bordered Hessian descriptor (D) is represented by*

$$D = \frac{\max(\det B) - \min(\det B)}{|mean(\det B)| + \varepsilon} \tag{7}$$

where B denotes the corresponding bordered Hessian structure and ε is a small numerical stabilization term.

Definition 7. *Let the fitted polynomial representation be expressed implicitly as $F(x, y) = y - f(x)$. The corresponding first- and second-order partial derivatives are $F_x = -f'(x)$, $F_y = 1$, $F_{xx} = -f''(x)$, and $F_{xy} = F_{yx} = F_{yy} = 0$. Then the bordered Hessian matrix is*

$$B_F = \begin{pmatrix} 0 & F_x & F_y \\ F_x & F_{xx} & F_{xy} \\ F_y & F_{yx} & F_{yy} \end{pmatrix} \tag{8}$$

and the gradient of the function $F(x,y)$ *is* $\nabla F = \left(\frac{\partial F}{\partial x}, \frac{\partial F}{\partial y}\right) = (-f'(x), 1)$*; here,* $F(x,y) = y - f(x)$ *is a continuous and derivable implicit function.*

Definition 8. *According to the mentioned calculations, the magnitude (norm) of the gradient is*

$$G(x) = \|\nabla F(x,y)\| = \sqrt{[f'(x)]^2 + 1}. \tag{9}$$

The resulting five-dimensional representation allows each rolling window to be treated as a point in a geometric feature space rather than merely as a sequence of scalar pressure observations.

Lemma 1 (Degeneracy of the bordered Hessian redistribution descriptor for a quadratic representation)**.** *Let the fitted local polynomial be expressed implicitly as* $F(x,y) = y - f(x) = 0$ *and let the bordered Hessian matrix be*

$$B_F = \begin{pmatrix} 0 & F_x & F_y \\ F_x & F_{xx} & F_{xy} \\ F_y & F_{yx} & F_{yy} \end{pmatrix}$$

with are $F_x = -f'(x)$, $F_y = 1$, $F_{xx} = -f''(x)$, *and* $F_{xy} = F_{yx} = F_{yy} = 0$.

If function f is quadratic, then $\det(B_F)$ is constant along the fitted segment. Consequently, any bordered Hessian descriptor D defined as the redistribution or dynamic variation in $\det(B_F)$ about its segment-wise mean is identically zero (up to numerical stabilization and round-off).

Proof. For $F(x,y) = y - f(x)$, direct expansion of the bordered Hessian determinant gives

$$\det(B_F) = f''(x).$$

For a quadratic polynomial $f(x) = ax^2 + bx + c$, a, b, c are real, one has $f''(x) = 2a$, which is independent of x. Hence $\det(B_F)$ is constant throughout the segment and equals its own segment-wise mean. Therefore, its redistribution about that mean, and hence the corresponding variation descriptor D, vanishes. □

Remark 1. *(Complementary roles of the five-dimensional signature).*

The signature $\mathbf{S} = (K, G, D, L_2, C_{KG})$ should be interpreted as a deliberately heterogeneous geometric representation. K and G summarize curvature- and gradient-related variation; D records redistribution in the bordered Hessian determinant; L_2 summarizes variation in the second eigenvalue of the associated geometric matrix; and C_{KG} records coupling between curvature and gradient. Thus, the five coordinates are designed to encode distinct but complementary aspects of local geometry. This construction does not assert that the five-dimensional signature is unique or minimal; rather, it provides a compact set of nonidentical geometric roles without using blind set information for feature selection.

3.5. Rolling-Window Construction

The geometric signature is calculated over consecutive overlapping windows.

Definition 9. *For a window length W, the s-th rolling window contains*

$$\mathcal{W}_s = \{P_s, P_{s+1}, \ldots, P_{s+W-1}\}. \tag{10}$$

A geometric signature is independently calculated for every window and for each polynomial degree d ∈ {2,3,4}.

Thus, each temporal window is associated with three geometric signatures,

$$\boldsymbol{S}_{s,2}, \boldsymbol{S}_{s,3}, \boldsymbol{S}_{s,4} \tag{11}$$

This construction permits the temporal evolution of the signal to be studied as a trajectory through geometric feature space.

3.6. Robust Normalization of the Geometric Feature Space

Because the five geometric descriptors may have substantially different numerical scales, robust scaling [18] is applied before calculating geometric distances. Robust scaling is preferred because the geometric descriptors can exhibit strongly skewed distributions and occasional large ratios. Median and interquartile-range-based normalization reduces the influence of extreme descriptor values compared with conventional mean and standard deviation scaling.

For each polynomial degree, the scaling transformation is fitted exclusively to the normal and anomalous reference populations.

Definition 10. *The blind observations are transformed using the parameters obtained from these reference populations but are never used in fitting the scaling transformation. Thus,*

$$X_{\text{ref}} = X_N \cup X_A \tag{12}$$

where X_N and X_A denote the normal and anomalous reference signatures, respectively.

The blind set X_M is subsequently transformed using the same scaling parameters.

This separation is essential because the blind observations must not influence the construction of the reference geometric space.

3.7. Empirical Reference Manifolds

The normal and anomalous reference observations are subsequently used to construct empirical geometric reference structures.

For each polynomial degree, the local density of the normal reference population is characterized through a same-class k-nearest-neighbor radius [19]. For a reference point x_i, the distance to its k-th nearest neighbor within the same reference class is calculated. The neighborhood size is fixed at $k = 7$ throughout the analysis. This value is used as a predefined local neighborhood scale rather than as an optimized hyperparameter. The purpose is to characterize local reference geometry using several neighboring observations, thereby reducing dependence on a single nearest reference point while retaining a sufficiently local description of the empirical N and A structures. The same value of k is applied to both reference populations, all three Bézier degrees, and every blind rolling window; no information from the blind set is used to select or modify k. Consequently, the reported manifold relationships reflect a fixed and symmetric neighborhood rule rather than window-specific parameter tuning.

Definition 11. *Let z denote the robust scaled geometric signature of a blind window. Its distances to the k-th nearest observations in the N and A reference populations are denoted by $d_N(z)$ and $d_A(z)$, respectively. For the normal reference manifold*

$$d_N(z) = \left\| z - z_{(k)}^{(N)} \right\|_2 \tag{13}$$

and

$$d_A(z) = \|z - z_{(k)}^{(A)}\|_2 \tag{14}$$

here $z_{(k)}^{(A)}$ and $z_{(k)}^{(A)}$ are in a robust-scaled geometric-signature space; z is the k-th nearest neighbor in the relevant reference population. kNN is a standard neighborhood-based method [19]. The corresponding notation for the normal reference set N is defined analogously. Throughout the primary analysis, $k = 7$.

The resulting collection of radii defines an empirical density envelope for the corresponding reference population.

The same procedure is independently applied to the anomalous reference population.

Importantly, the blind observations do not participate in the construction of either reference envelope. They are evaluated only after the normal and anomalous reference structures have been established.

3.8. Blind Geometric Distance

Definition 12. *For every blind rolling window, two independent distances are calculated:*

$$d_N = d_k(X_M, X_N) \tag{15}$$

and

$$d_A = d_k(X_M, X_A) \tag{16}$$

where d_k denotes the Euclidean distance to the k-th nearest reference observation.

The resulting pair,

$$(d_N, d_A) \tag{17}$$

provides a relative geometric position of the blind observation with respect to the normal and anomalous reference structures.

This formulation is deliberately different from direct classification. A blind observation can simultaneously lie within both empirical envelopes, outside both envelopes, or within only one of them.

Accordingly, four states are considered:

		Inside N	**Inside A**
i. N-manifold member	N-member	1	0
ii. A-manifold member	A-member	0	1
iii. overlap	overlap	1	1
iv. novel/transition	novel/transition	0	0

95th percentile is adopted as a fixed empirical coverage criterion for defining the outer neighborhood envelope of each reference population. It is not interpreted as a 95% confidence interval or as a parametric probability bound. Rather, the percentile provides a robust data-driven boundary derived directly from the distribution of same-class *k*NN radii, retaining the predominant reference geometry while limiting the influence of unusually large neighborhood distances.

Definition 13. *The threshold is not given externally as an arbitrary physical threshold:*

$$\begin{array}{l} r_1^{(N)}, \ldots, r_n^{(N)} \longrightarrow Q_{0.95}^N \\ r_1^{(A)}, \ldots, r_n^{(A)} \longrightarrow Q_{0.95}^A \end{array} \tag{18}$$

here r_i^N and r_i^A are the distances to the k-th nearest neighbor within the same class for each reference observation. That is, the limit comes from the same-class kNN-radius distribution of the reference population. The same percentile criterion is applied symmetrically to the N and A reference populations and to all Bézier degrees. As with the neighborhood size, the envelope percentile is fixed independently of the blind set and is not adjusted according to the resulting blind window classifications. Explicitly,

$$\begin{aligned} T_N &= Q_{0.95}(\{r_i^N\}_{i=1}^{n_N}) \\ T_A &= Q_{0.95}(\{r_i^A\}_{i=1}^{n_A}) \end{aligned} \tag{19}$$

For the blind z,

$$\begin{aligned} z \in E_N &\iff d_N(z) \le T_N \\ z \in E_A &\iff d_A(z) \le T_A \end{aligned} \tag{20}$$

These states describe geometric proximity to the empirical reference structures and should not be interpreted as direct physical labels.

3.9. Directional Manifold Score

Definition 14. *For the present framework, the directional manifold score is defined as the logarithmic distance ratio (Φ):*

$$\Phi = \log\left(\frac{d_N + \epsilon}{d_A + \epsilon}\right). \tag{21}$$

For each polynomial degree $d \in \{2,3,4\}$, the five-dimensional geometric signature is expressed as $\boldsymbol{S}_d = (K, G, D, L_2, C_{KG})$. Because these descriptors may have different numerical magnitudes and skewed distributions, a feature-wise robust scaling transformation is applied before computing Euclidean distances.

The scaling parameters are estimated exclusively from the pooled normal and anomalous reference signatures, $X_{\mathrm{ref},d} = X_{\mathrm{N},d} \cup X_{\mathrm{A},d}$. For each feature $j = 1, \ldots, 5$, the reference median $m_{j,d}$ and interquartile range $\mathrm{IQR}_{j,d} = Q_{0.75,j,d} - Q_{0.75,j,d}$ are calculated. Each signature component is then transformed according to $\tilde{S}_{j,d} = (S_{j,d} - m_{j,d})/\mathrm{IQR}_{j,d}$.

The same degree-specific transformation is applied to the normal, anomalous, and blind signatures. Importantly, the blind dataset is not used to estimate or update the scaling parameters. All subsequent nearest-neighbor distances and empirical reference-envelope thresholds are computed in the resulting robust-scaled geometric feature space. This procedure reduces the influence of differences in feature magnitude while preserving the independence of the blind evaluation from reference calibration.

Proposition 1 (Symmetry and scale invariance of the directional manifold score)**.** *Let $d_N > 0$ and $d_A > 0$ denote the distances of a blind geometric signature to the normal and anomalous reference structures, respectively, and define*

$$\Phi = \ln\left(\frac{d_N}{d_A}\right)$$

Then the following properties hold:

i. $\Phi = 0$ *if and only if* $d_N = d_A$,
ii. $\Phi > 0$ *if and only if* $d_N > d_A$ *and* $\Phi < 0$ *if and only if* $d_N < d_A$,
iii. Exchanging the two reference distances reverses the sign, $\Phi(d_N, d_A) = -\Phi(d_A, d_N)$ *and*
iv. For every common scale factor $c > 0$, $\Phi(cd_N, cd_A) = \Phi(d_N, d_A)$.

Proof . Because the natural logarithm is strictly increasing, $\ln\left(\frac{d_N}{d_A}\right) = 0$ exactly when $\frac{d_N}{d_A} = 1$, proving (i). The same monotonicity gives the sign relations in (ii). For (iii),

$$\ln\left(\frac{d_A}{d_N}\right) = \ln\left[\left(\frac{d_N}{d_A}\right)^{-1}\right] = -\ln\left(\frac{d_N}{d_A}\right)$$

Finally, for $c > 0$,

$$\ln[(cd_N)/(cd_A)] = \ln(d_N, d_A)$$

which provides (iv).

According to this formula, when the ratio is zero, the two distances are equal; positive and negative values indicate relative proximity toward the anomalous and normal reference structures, respectively.

The sign of Φ provides the directional interpretation.

$$\Phi > 0 \Rightarrow \text{ relative movement toward the anomalous reference,}$$

whereas

$$\Phi < 0 \Rightarrow \text{ relative movement toward the normal reference.}$$

Importantly, a positive value does not imply anomalous-manifold membership. It indicates only that the observation is relatively closer to the anomalous reference structure than to the normal reference structure.

This distinction is fundamental to the proposed framework. □

3.10. Polynomial-Degree Consensus

Because the same rolling window is represented independently using quadratic, cubic, and quartic Bézier approximations, the directional scores obtained from the three polynomial degrees can be compared.

For each temporal window,

$$\Phi_2,\ \Phi_3,\ \Phi_4 \tag{22}$$

are evaluated.

A degree-consensus measure is then defined according to the signs of these three directional scores. A positive contribution is assigned when the corresponding degree indicates movement toward the anomalous reference, while a negative contribution is assigned when it indicates movement toward the normal reference.

Definition 15 (Cross-degree directional consensus index)**.** *For each rolling window (s), let $\Phi_{\{s,d\}}$ denote the directional manifold score obtained from the Bézier representation of degree $d \in \{2,3,4\}$. The cross-degree directional consensus index is defined as*

$$C_A(s) = \sum_{d=2}^{4} sgn(\Phi_d) \tag{23}$$

where $C_A(s) = sgn(\Phi_{s,2}) + sgn(\Phi_{s,3}) + sgn(\Phi_{s,4})$. When all three directional scores are nonzero, $C_A(s) \in \{-3, -1, +1, +3\}$. The four nonzero-score consensus states are interpreted as follows:

i. $(C_A(s) = +3)$: unanimous anomalous-direction consensus,
ii. $(C_A(s) = +1)$: weak anomalous-direction consensus, supported by two of the three polynomial degrees,
iii. $(C_A(s) = -1)$: weak normal-direction consensus, supported by two of the three polynomial degrees,
iv. $(C_A(s) = -3)$: unanimous normal-direction consensus.

If one or more directional scores are zero, the corresponding degree contributes zero to the index, indicating equal distances to the normal and anomalous reference structures. Such cases are treated as neutral contributions rather than being assigned an anomalous or normal direction.

The index measures directional agreement across polynomial degrees and does not, by itself, establish exclusive membership in either empirical reference manifold or identify a physical disturbance.

Proposition 2 (Cross-degree consensus property)**.** *For the three Bézier degrees $d \in \{2,3,4\}$, let Φ_d be the corresponding directional manifold scores and assume $\Phi_d \neq 0$. Define the cross-degree consensus index by*

$$C_A = sgn(\Phi_2) + sgn(\Phi_3) + sgn(\Phi_4).$$

Then $C_A \in \{-3, -1, +1, +3\}$. Moreover, $|C_A| = 3$ if and only if all three polynomial degrees have the same directional sign. In particular, $C_A = +3$ if and only if $\Phi_2 > 0$, $\Phi_3 > 0$, $\Phi_4 > 0$; similarly, $C_A = -3$ if and only if all three scores are negative.

Proof. Under the nonzero-score assumption, each sign term belongs to $\{-1, +1\}$. The sum of three such terms can therefore take only the values -3, -1, $+1$, or $+3$. A magnitude of three is possible only when all three terms have the same sign; conversely, three equal signs sum to $+3$ or -3. The stated equivalences follow immediately. □

The consensus procedure therefore asks whether the detected directional behavior persists across alternative polynomial representations rather than relying on a single fitted curve.

3.11. Temporal Persistence and Transition Detection

The final stage examines the temporal persistence of the directional geometric signal.

Definition 16. *For consecutive rolling windows, the mean directional score is calculated as*

$$\overline{\Phi}_s = \frac{\Phi_{s,2} + \Phi_{s,3} + \Phi_{s,4}}{3}. \tag{24}$$

Its temporal change is subsequently evaluated as

$$\Delta\overline{\Phi}_s = \overline{\Phi}_s - \overline{\Phi}_{s-1} \tag{25}$$

A successive change in the mean directional manifold score is considered geometrically persistent when a sequence of neighboring windows exhibits a coherent change in directional state, particularly when the transition is supported by multiple polynomial degrees.

In the final blind sequence investigated here, two consecutive strong normal-direction windows are followed by a weak anomalous-direction window and subsequently by three consecutive strong anomalous-direction windows. The final window exhibits positive consensus across all three polynomial degrees.

This temporal persistence constitutes the principal geometric transition signature of the proposed framework.

3.12. Separation of Geometric Detection from Physical Interpretation

The proposed methodology intentionally separates structural detection from physical attribution.

The geometric framework identifies whether the temporal signal exhibits a persistent structural transition relative to empirically constructed reference geometries. It does not, by

itself, determine whether the physical origin of that transition is associated with a particular solar wind structure, interplanetary disturbance, shock, coronal mass ejection-related event, or geomagnetic response.

Such physical attribution requires independent examination of the relevant solar wind and geomagnetic parameters.

This separation allows the geometric method to function as a complementary structural-detection framework rather than as a replacement for conventional space weather interpretation.

4. Results and Discussion

4.1. Geometric Characterization Across Polynomial Degrees

The proposed framework is applied to the dynamic pressure time series by representing each rolling temporal segment through quadratic, cubic, and quartic Bézier polynomial descriptions. For each degree, the resulting curve is transformed into a five-dimensional geometric signature composed of curvature, gradient, bordered Hessian, eigenvalue, and curvature-gradient-correlation-based descriptors. The use of three polynomial degrees is intended to determine whether the detected structural behavior depended strongly on a particular polynomial representation or whether it persisted across alternative local descriptions.

The geometric representation does not produce identical numerical responses for all polynomial degrees, as expected from the different flexibility and local approximation properties of quadratic, cubic, and quartic Bézier curves. Nevertheless, the directional information extracted from these representations becomes substantially more coherent in the final part of the blind sequence. The principal criterion is therefore not equality of the descriptor magnitudes across degrees, but persistence of the inferred direction when the same temporal window is represented by alternative polynomial descriptions.

Figure 1 illustrates the piecewise Bézier representation of the observed dynamic pressure (nPa) sequences and demonstrates how the quadratic, cubic, and quartic models reproduce the local temporal structure of the data.

The fitting error decreases systematically with increasing polynomial degree for all three datasets, reflecting the greater local flexibility of the higher-degree representations. Nevertheless, the subsequent analysis does not select a single optimal degree; instead, quadratic, cubic, and quartic representations are retained jointly to evaluate cross-degree persistence of the geometric transition.

4.2. Empirical Normal and Anomalous Geometric Reference Structures

For each polynomial degree, the five-dimensional signatures of the normal and anomalous reference populations are robustly scaled using only the reference observations. The blind observations are subsequently transformed with the same scaling parameters and are therefore prevented from influencing the construction of the reference geometric space. This separation preserves the blind character of the final observations and avoids circularity in the geometric comparison.

The empirical reference structures are characterized using same-class k-nearest-neighbor radii. The resulting 95th-percentile envelope thresholds are 2.009713 for the normal reference and 17.197167 for the anomalous reference at degree 2; 7.766406 and 17.221534, respectively, at degree 3; and 16.540233 and 18.620816 at degree 4. These values demonstrate that the empirical density structure differs among polynomial degrees and between the two reference populations. Accordingly, the method does not assume a common geometric scale or a common reference density for normal and anomalous states.

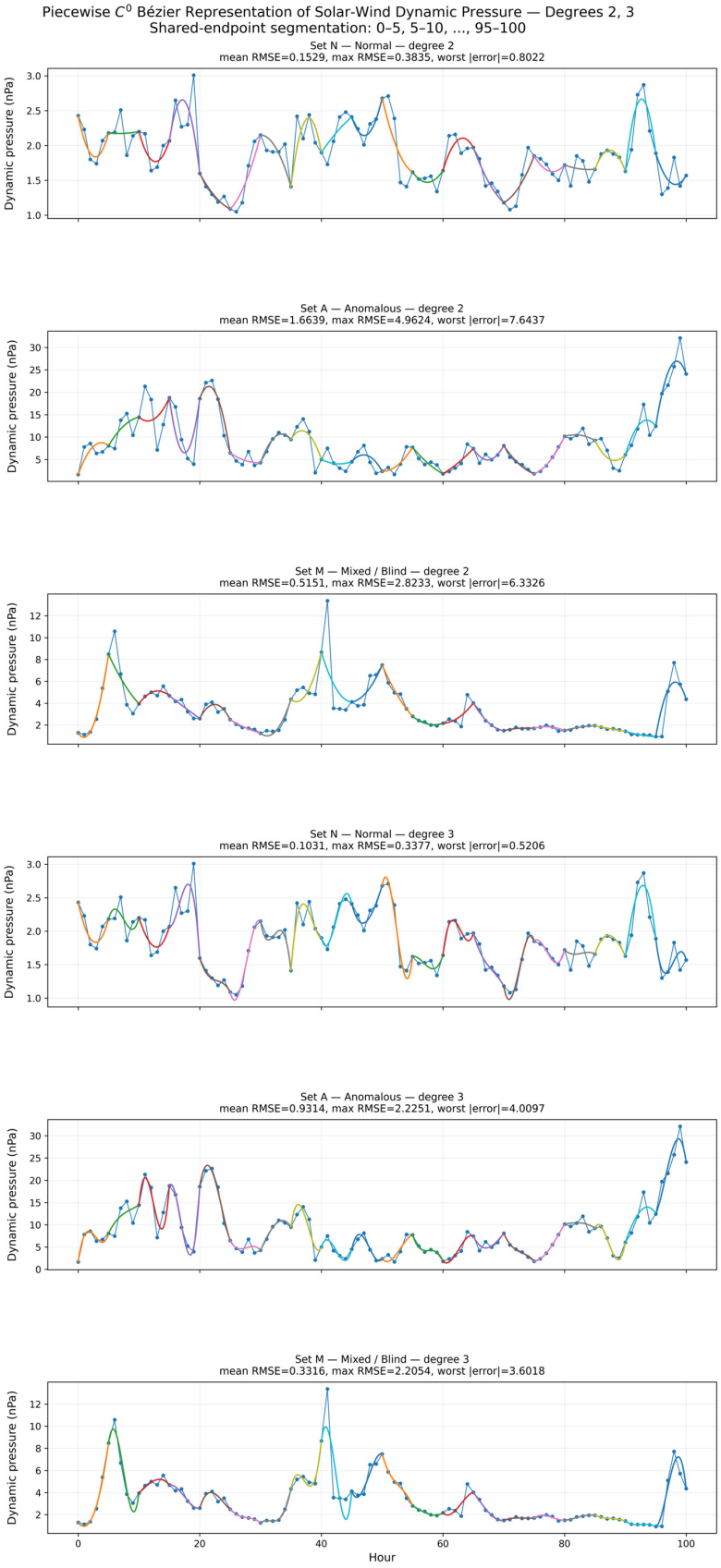


Figure 1. *Cont*.

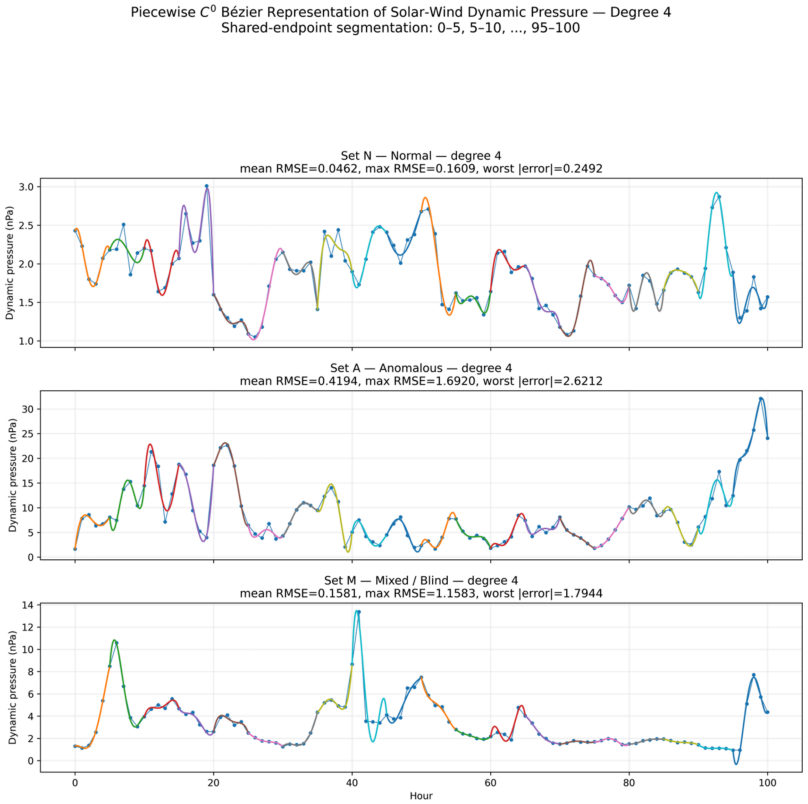


Figure 1. Piecewise C^0 continuous Bézier representations of the normal (N), anomalous (A), and mixed/blind (M) dynamic pressure sequences using quadratic, cubic, and quartic polynomial degrees. Shared-endpoint segmentation is applied over the intervals 0–5, 5–10, ..., 95–100, with $B_i(1) = B_{i+1}(0)$. The panels report the mean segment RMSE, maximum segment RMSE, and worst absolute fitting error for each dataset and polynomial degree.

The differences between the normal and anomalous reference-envelope thresholds reflect differences in the empirical distributions of their five-dimensional geometric signatures. The envelopes are constructed separately for each reference population and polynomial degree using the 95th percentile of same-class k-nearest-neighbor radii in the robustly scaled feature space. Consequently, a larger threshold indicates a larger upper-tail local-neighborhood scale and is consistent with a more dispersed or heterogeneous reference configuration. In particular, the anomalous-to-normal threshold ratio decreases from approximately 8.56 for the quadratic representation to 2.22 for the cubic representation and 1.13 for the quartic representation. This degree dependence indicates that the separation of the empirical neighborhood scales is representation-dependent rather than a universal property of the underlying plasma states. Importantly, these thresholds are not probability-based confidence limits, direct estimates of physical plasma density, or interchangeable measures of absolute population density. They are operational geometric boundaries calibrated independently for the two reference populations. Their differences therefore do not introduce a requirement that normal and anomalous states occupy equally dense regions of feature space, nor do they establish the physical origin of the observed geometric differences.

Figure 2 illustrates the curvature and gradient magnitude behavior of different Bézier models on the same last blind window.

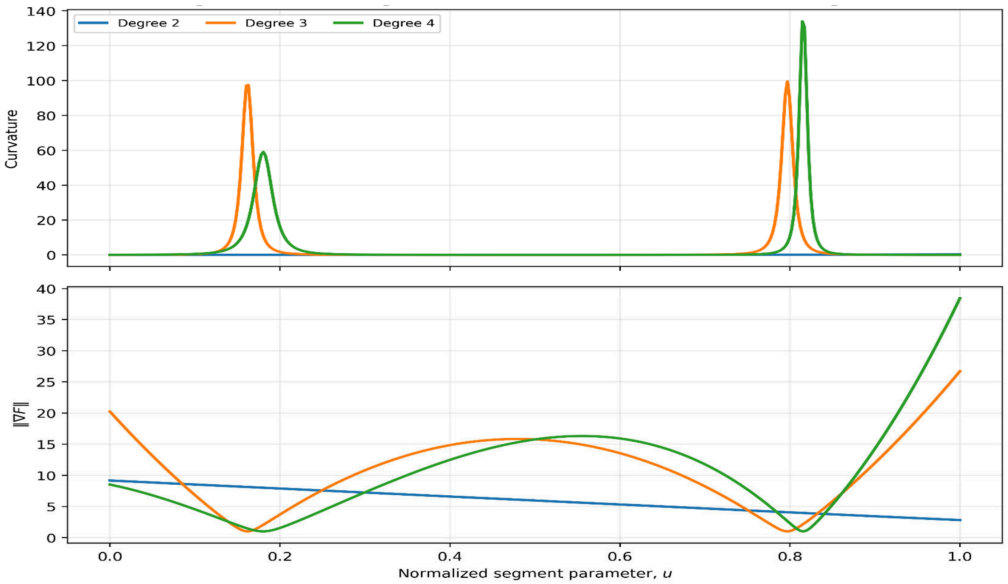


Figure 2. Differential geometric characterization of the final blind segment.

Figure 2 compares the curvature and gradient-magnitude responses obtained from the quadratic, cubic, and quartic representations of the final blind window. The differences among the three polynomial degrees reflect their distinct local flexibility, while the common temporal interval permits direct comparison of the corresponding differential geometric responses.

4.3. Blind-Window Manifold Relationships

The blind observations are evaluated only after the reference structures have been established. A blind window is therefore not assigned an anomalous label solely because its directional score is positive. Instead, its distances to the normal and anomalous reference structures are examined jointly with its empirical-envelope membership. This distinction results in four geometric states: normal-manifold member, anomalous-manifold member, overlap, and novel/transition.

For the final blind window, 93–100, the degree-specific distances are 0.612464 to the normal reference and 0.132804 to the anomalous reference for degree 2, 1.888866 and 1.481330 for degree 3, and 1.266756 and 0.556335 for degree 4. The final blind window is directionally closer to the anomalous reference structure for all three polynomial degrees, while remaining within an overlap state in terms of empirical-envelope membership. This result is methodologically important: the analysis detects persistent directional movement toward the anomalous reference without claiming that the blind window has necessarily entered an exclusively anomalous manifold.

Figure 3 shows the representation of geometric distances or manifold structure relative to normal and anomalous reference structures. Figure 3 may also be presented as the position of N/A reference structures and blind M windows in robust-scaled geometric space, along with the temporal evolution of *k*NN distances to N and A references. In Figure 3, principal component analysis (PCA) is utilized solely to provide a two-dimensional visualization of the robust-scaled geometric feature space; neither reference-manifold construction nor *k*NN distance computation is performed in the PCA-projected space [20].

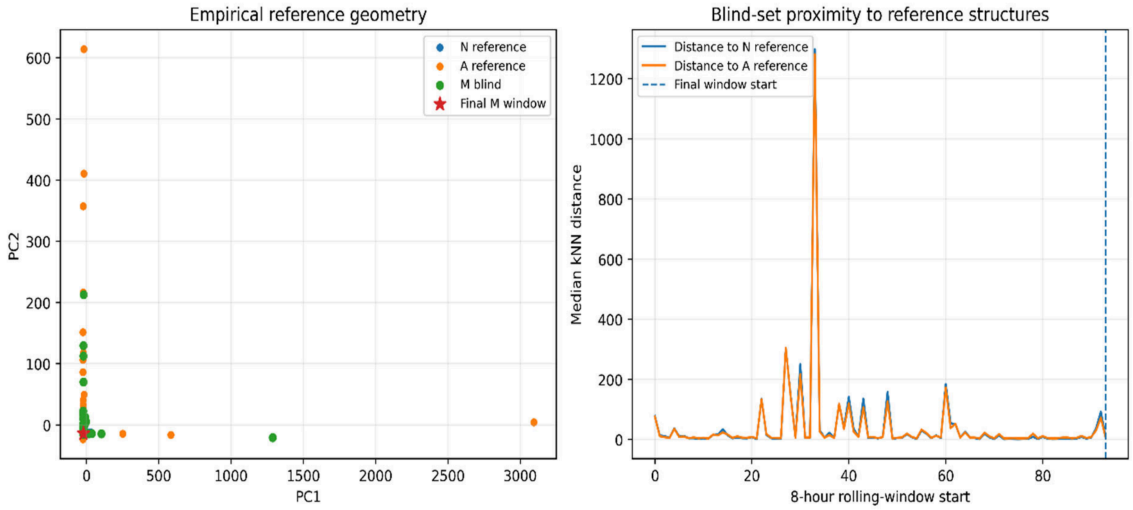


Figure 3. Empirical N/A reference geometry, PCA visualization, and blind-window *k*NN distances.

The overlap state observed for the final blind window does not contradict its positive anomalous-direction scores. These two outcomes describe different geometric properties. The directional score compares relative proximity to the normal and anomalous reference structures, whereas envelope membership evaluates whether the corresponding distances satisfy the two independently calibrated reference thresholds.

Specifically, a positive directional score indicates that the blind signature is closer to the anomalous reference structure than to the normal reference structure. However, exclusive anomalous-envelope membership additionally requires the signature to lie within the anomalous envelope and outside the normal envelope. When both envelope conditions are satisfied, the signature is assigned to the overlap state, regardless of which reference structure is closer.

For the final blind window (93–100), the three polynomial degrees consistently indicate relative proximity to the anomalous reference. Nevertheless, the distances remain within both empirical reference envelopes. Consequently, the result is interpreted as unanimous anomalous-direction consensus within an overlapping geometric region, rather than as exclusive anomalous-manifold membership.

This distinction is important because the empirical reference envelopes are not assumed to be mutually exclusive. Their overlap reflects the fact that normal and anomalous reference signatures may occupy partially shared regions of the geometric feature space. Therefore, the proposed framework identifies a directional structural transition relative to the reference populations without claiming a definitive physical event classification.

4.4. Directional Transition in the Final Rolling Sequence

The most informative result is obtained from the temporal sequence of directional manifold scores. In the final portion of the blind sequence, windows 88–95 and 89–96 exhibit strong normal-direction consensus, with mean scores of −1.117992 and −1.159568, respectively. The subsequent window, 90–97, changes to a weak anomalous-direction state, with degree-specific scores of 1.210255, −0.041381, and 0.156505 and a mean score of 0.441793. This is followed by three consecutive strong anomalous-direction windows: 91–98, 92–99, and 93–100.

The transition is particularly pronounced between windows 89–96 and 90–97, where the mean directional score, $\overline{\Phi}$, changes by 1.601361. The following changes are smaller but remain positive: 0.283177, 0.125588, and 0.014276 for the transitions into windows 91–98, 92–99, and 93–100, respectively. The sequence therefore contains not merely an

isolated positive score, but a change from successive normal-direction states to successive anomalous-direction states followed by persistence of the positive state. Figure 4 represents the transition of quadratic, cubic, quartic, and mean directional manifold scores through the final rolling sequence.

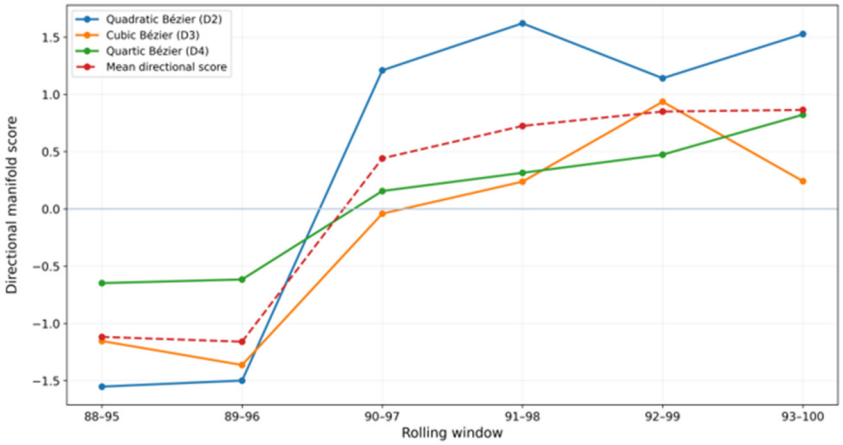


Figure 4. Final N–to–A (normal to anomalous) geometric transition signature.

The proposed framework does not merely identify an isolated anomalous observation; rather, it detects a persistent directional transition across neighboring temporal windows and alternative polynomial representations. Figure 4 visualizes the degree-specific directional scores and their mean over the terminal rolling sequence, making the change from N-directed to A-directed geometry directly observable across neighboring windows.

4.5. Polynomial-Degree Consensus

The degree-consensus analysis provides an additional test of structural persistence. For windows 88–95 and 89–96, all three polynomial degrees produced negative directional scores, yielding a consensus value of −3. For window 90–97, the consensus changed to +1, reflecting a transitional state in which the degree-specific representations are not yet fully aligned. The next three windows, 91–98, 92–99, and 93–100, all reached a consensus value of +3.

The final window therefore exhibits unanimous positive directional consensus across quadratic, cubic, and quartic representations. This agreement is significant within the logic of the proposed framework because it indicates that the detected final directional transition is not attributable to one selected polynomial degree. The degree-consensus criterion consequently strengthens the interpretation of the transition as a structural property of the represented signal rather than an artifact of a single polynomial approximation. Figure 5 displays the evolution of the cross-degree consensus during the terminal transition.

According to Figure 5, the consensus score combines the directional indications obtained independently from quadratic, cubic, and quartic Bézier representations. Negative values indicate normal-direction consensus, whereas positive values indicate anomalous-direction consensus. The final three windows exhibit unanimous positive consensus across all three polynomial degrees.

4.6. Persistent Normal (N)-to-Anomalous (A) Geometric Transition Signature

The resulting signature is therefore described as a persistent N-to-A geometric transition. Here, N-to-A denotes a directional transition in the geometric feature space from relative proximity toward the normal reference structure to relative proximity toward the anomalous reference structure. It does not denote a direct physical classification of the solar

wind event and does not imply that the final blind window is exclusively an anomalous-manifold member. Figure 6 displays temporal evolution of the mean directional manifold score during the final transition.

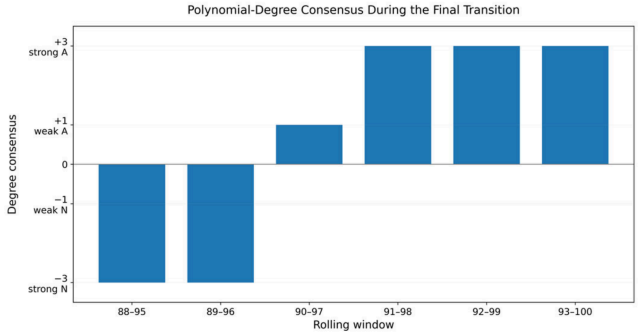


Figure 5. Polynomial-degree consensus during the final geometric transition.

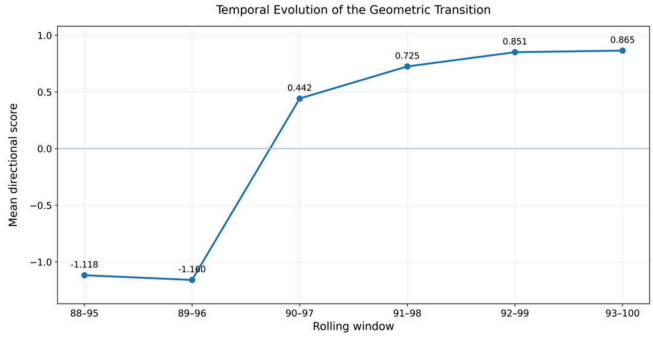


Figure 6. Temporal evolution of the geometric transition.

The terminal sequence consists of two consecutive strong normal-direction windows, followed by one weak anomalous-direction window and three consecutive strong anomalous-direction windows. The final window, 93–100, has degree-specific scores of 0.721398, 0.253658, and 0.742093, yielding a mean directional score of approximately 0.572383 and a unanimous degree consensus of +3.

The terminal sequence exhibits a coherent directional transition, characterized by two consecutive windows with unanimous normal-direction consensus, followed by a transitional window and three consecutive windows with unanimous anomalous-direction consensus. This pattern is preserved under the additional neighborhood setting of $k = 5$, while $k = 7$ remains the predefined primary setting. The agreement across polynomial degrees provides descriptive evidence of directional consistency. Nevertheless, the rolling windows overlap substantially, and the degree-specific signatures are derived from the same observations. Consequently, the observed consensus should not be interpreted as a sequence of statistically independent events. The present results establish a persistent directional pattern relative to the constructed reference populations, but do not establish its statistical significance under a validated stochastic null model.

4.7. Interpretation and Methodological Implications

The results support the central hypothesis of the study: a structurally persistent transition in a time-domain solar wind signal can leave a detectable trace after the signal is represented in an alternative geometric feature space. The persistence is supported simultaneously by temporal continuity and by agreement among polynomial degrees. This provides a complementary perspective to conventional signal analysis, in which changes

are commonly evaluated directly through amplitude, statistical thresholds, or frequency-domain characteristics.

At the same time, one needs to interpret the present consequences within the scope of the mathematical framework. The geometric analysis identifies a persistent structural transition, but it does not establish whether the transition is physically generated by a shock, a coronal mass ejection, a stream interaction, a magnetic disturbance, or another solar wind process. Such attribution must be established independently using the relevant physical parameters and event information. This separation between mathematical detection and physical attribution is intentional and allows the proposed framework to serve as a structural-detection layer that can be combined with conventional space weather analysis.

The analysis also suggests that the proposed geometric representation may be extended beyond dynamic pressure. Because the framework is based on the mathematical representation of an ordered time-domain signal rather than on a parameter-specific physical equation, related solar wind variables such as proton density can be investigated using the same conceptual procedure. More complex geophysical observations may subsequently be examined after the behavior of the framework has been established for fundamental solar wind parameters.

From a broader methodological perspective, the central question is whether the structural character of a time-domain signal remains detectable after the signal is mapped into an alternative geometric representation. The present results suggest that the relative normal-to-anomalous organization of the reference data is not lost under this transformation; rather, it becomes expressible through distances, directional scores, and cross degree persistence in the constructed geometric feature space. Tables 2 and 3 summarize this relationship quantitatively by showing that different polynomial representations yield different numerical distances while preserving a coherent terminal directional interpretation. Table 2 shows that three different polynomial representations have three different numerical equivalents within the same final routing context. Table 3 demonstrates this consensus.

Table 2. Degree-specific empirical envelope thresholds and final window manifold distances and directional scores.

Degree	N Threshold 95% Envelope	A Threshold 95% Envelope	Final d_N	Final d_A	Final Score ($\Phi_d = \ln(d_N/d_A)$)
2	2.009713	17.197167	0.617467	0.300133	0.721398
3	7.766406	17.221534	1.940961	1.506102	0.253658
4	16.540233	18.620816	1.248069	0.594226	0.742093

Table 3. Terminal directional degree-consensus states.

Window	Mean Score	Consensus	State
88–95	−1.117992	−3	Strong N
89–96	−1.159568	−3	Strong N
90–97	0.441793	+1	Weak A
91–98	0.724970	+3	Strong A
92–99	0.850558	+3	Strong A
93–100	0.572383	+3	Strong A

For the final window (93–100), the mean directional score across the three Bézier degrees is $\overline{\Phi} = 0.572383$. The 95th percentile thresholds represent empirical reference envelope boundaries rather than probabilistic confidence intervals.

4.8. Sensitivity Analysis of Geometric Transition Indicators

As a complementary fitting-method sensitivity experiment, the geometric descriptors are recomputed using C^0-continuous Bézier representations. This supplementary procedure differs from the unconstrained polynomial fitting employed in the primary rolling-window analysis; consequently, its numerical directional scores are not expected to coincide exactly with those reported in Table 2.

To examine the robustness of the geometric transition indicators, a supplementary sensitivity analysis is conducted using window lengths of 6–10 observations, nearest-neighbor values of k = 5, 7, and 9, and reference-envelope percentiles of 90%, 95%, and 97.5%, separately for quadratic, cubic, and quartic Bézier representations. All geometric descriptors are consistently derived from a single endpoint-constrained Bézier representation within each window. Among the resulting 135 configurations, 108 yield positive final blind-window directional scores. For the primary eight-observation configuration, all 27 combinations of polynomial degree, nearest-neighbor parameter, and envelope percentile retain positive directional scores. At k = 7 and the 95% envelope, the final-window scores are 1.0494, 0.0540, and 0.7383 for degrees 2, 3, and 4, respectively. Nevertheless, exclusive anomalous-envelope membership is observed only for the quadratic representation, while the cubic and quartic representations remain within overlapping reference envelopes. Furthermore, some alternative window lengths reverse the directional-score sign. These results indicate conditional robustness of the directional geometric indication, rather than complete invariance to the analytical parameters.

Several methodological considerations define the scope of the present results. The eight-observation rolling window, the neighborhood size ($k = 7$), and the 95th percentile empirical envelope are adopted as fixed operational parameters rather than optimized or physically unique values. Accordingly, the current analysis ought to be interpreted as evidence of a persistent geometric transition relative to the constructed normal and anomalous reference populations, rather than as proof of a universal classification boundary. Moreover, geometric proximity to a reference manifold does not by itself establish the physical cause of the observed transition. Although three independent calendar-year intervals are examined in Section 4.9, further validation using independently labeled physical events, explicitly defined quiet-time controls, and suitable confirmatory null-model tests is required to quantify false-positive behavior and establish statistical detection performance.

4.9. Independent Out-of-Sample Validation Across Three Calendar Years

To examine the out-of-sample consistency of the proposed geometric framework, three additional solar wind dynamic pressure records are evaluated, corresponding to 1–5 January in 2021, 2022, and 2023. Each record comprises 101 consecutive hourly observations and is partitioned into 94 overlapping eight-observation windows.

The original normal (N) and anomalous (A) reference populations are retained without recalibration. The same five-dimensional geometric signature, reference-based robust scaling, seventh-nearest-neighbor distance (k = 7), and 95th-percentile reference envelopes are applied to each independent record.

The 2021 and 2022 records exhibit no windows with unanimous anomalous-direction consensus across polynomial degrees 2, 3, and 4. In contrast, eight windows in the 2023 record exhibit unanimous anomalous-direction consensus. These windows are concentrated in two temporally localized groups and are associated with pronounced variations in the observed dynamic pressure.

The numbers of windows exhibiting unanimous normal-direction consensus are 84, 88, and 67 for 2021, 2022, and 2023, respectively. These findings indicate that the geometric responses are not uniformly distributed across the independent validation records.

Nevertheless, unanimous anomalous-direction consensus represents relative proximity to the anomalous reference geometry and does not, by itself, establish an independently verified physical event. Because the windows overlap and independent event/non-event labels are unavailable, formal false-positive and false-negative rates cannot be reliably estimated from these results. The findings therefore provide evidence of out-of-sample geometric consistency rather than definitive event-detection accuracy.

As shown in Table 4, the eight anomalous-direction consensus windows are concentrated within two temporally localized groups on 3–4 January 2023. The first group encompasses a pronounced pressure enhancement reaching 6.46 nPa, followed by a rapid decrease, whereas the second group coincides with a subsequent interval of substantial pressure variability, including a maximum value of 7.83 nPa. These observations indicate that the anomalous-direction geometric responses are temporally associated with pronounced changes in the measured dynamic pressure rather than being uniformly distributed throughout the validation record. Moreover, the absence of unanimous anomalous-direction consensus in the independent 2021 and 2022 records provides an encouraging contrast with the more variable 2023 interval. Nevertheless, because the windows overlap and no independent event labels have yet been established, these findings should be interpreted as evidence of out-of-sample geometric consistency and observational correspondence, not as a definitive estimate of event-detection performance or false-positive rates.

Table 4. Temporal correspondence between unanimous anomalous-direction geometric consensus and observed solar wind dynamic pressure in the independent 2023 validation interval (3–4 January 2023, UT).

Window	Start (UT)	End (UT)	Dynamic Pressure P (nPa)						Directional Score (Φ)			Consensus
			Start	End	Min	Max	Mean	Value	Φ_2	Φ_3	Φ_4	
68–75	01.03 20:00	01.04 03:00	2.55	1.86	1.86	6.46	4.200	2.55, 3.00, 4.23, 5.01, 5.13, 5.36, 6.46, 1.86	0.6307	0.7940	0.2072	3
70–77	01.03 22:00	01.04 05:00	4.23	1.19	1.06	6.46	3.788	4.23, 5.01, 5.13, 5.36, 6.46, 1.86, 1.06, 1.19	0.8414	0.9579	0.7996	3
71–78	01.03 23:00	01.04 06:00	5.01	1.09	1.06	6.46	3.395	5.01, 5.13, 5.36, 6.46, 1.86, 1.06, 1.19, 1.09	1.0704	0.3258	0.2286	3
73–80	01.04 01:00	01.04 08:00	5.36	2.48	1.06	6.46	2.651	5.36, 6.46, 1.86, 1.06, 1.19, 1.09, 1.71, 2.48	1.4825	0.5613	0.0459	3
81–88	01.04 09:00	01.04 16:00	2.34	7.74	1.25	7.83	3.525	2.34, 1.81, 1.55, 1.25, 1.68, 4.00, 7.83, 7.74	0.5073	0.4524	0.2023	3
83–90	01.04 11:00	01.04 18:00	1.55	3.89	1.25	7.83	4.149	1.55, 1.25, 1.68, 4.00, 7.83, 7.74, 5.25, 3.89	1.2935	1.0057	0.4102	3
84–91	01.04 12:00	01.04 19:00	1.25	4.42	1.25	7.83	4.508	1.25, 1.68, 4.00, 7.83, 7.74, 5.25, 3.89, 4.42	1.2409	0.0453	0.5288	3
85–92	01.04 13:00	01.04 20:00	1.68	3.79	1.68	7.83	4.825	1.68, 4.00, 7.83, 7.74, 5.25, 3.89, 4.42, 3.79	0.9813	0.6147	0.4751	3

Note: All reported windows contain eight hourly observations and exhibit a cross-degree consensus index of +3. Pressure extrema are calculated from the original OMNIWeb observations. Overlapping windows should not be interpreted as independent physical events. The results describe geometric directional agreement rather than independently verified event classification.

5. Conclusions

This study introduces a geometric-algebraic framework for investigating persistent structural transitions in solar wind dynamic pressure time series. The approach begins by retaining the observations in their original time-pressure representation and subsequently constructing local quadratic, cubic, and quartic Bézier representations. Differential geometric and polynomial-geometric descriptors are extracted from these representations and combined into a five-dimensional geometric signature.

Normal and anomalous reference populations are then used to construct empirical geometric reference structures. Blind observations are evaluated independently through their geometric distances to these structures, while robust normalization and reference-envelope construction are performed without using the blind observations. A logarithmic distance ratio is used to characterize the relative direction of movement, and a polynomial-degree consensus criterion is introduced to evaluate whether this direction persisted across alternative Bézier representations.

The final blind sequence reveals a coherent transition from strong normal-direction states to anomalous-direction states. The terminal sequence comprises two consecutive strong normal-direction windows, one weak anomalous-direction window, and three consecutive strong anomalous-direction windows. The final window, 93–100, produces positive directional scores for all three polynomial degrees and a unanimous +3 degree consensus, with a mean directional score of 0.572383.

These findings support the hypothesis that persistent structural changes in a solar wind time-domain signal can be detected through an alternative geometric representation. Importantly, the result is a directional geometric signature rather than a direct physical event classification. A positive movement toward the anomalous reference structure does not, by itself, establish anomalous-manifold membership or identify the physical mechanism responsible for the observed change.

The framework does not claim that geometry replaces physics; rather, it asks whether a temporal signal contains a persistent structural transition that becomes detectable after transformation into a geometric-algebraic representation. The principal contribution of the framework is therefore methodological: it provides an additional representation in which temporal signal evolution can be studied through geometric structure, reference manifolds, and cross-degree persistence. The approach may provide a basis for further investigations of other solar wind parameters, including proton density, and subsequently of more complex geophysical observations such as total electron content. Future work should combine the geometric signature with independent physical event identification and with algebraic analyses in order to determine how complementary geometric and algebraic structures can improve the characterization of space weather-related transitions.

Funding: This research received no external funding.

Data Availability Statement: The data presented in this study are openly available at https://omniweb.gsfc.nasa.gov/form/dx1.html (accessed on 24 August 2026).

Conflicts of Interest: The authors declare no conflict of interest.

References

1. Zhang, H.; Zong, Q.; Connor, H.; Delamere, P.; Facskó, G.; Han, D.; Hasegawa, H.; Kallio, E.; Kis, Á.; Le, G.; et al. Dayside transient phenomena and their impact on the magnetosphere and ionosphere. *Space Sci. Rev.* **2022**, *218*, 40. [CrossRef] [PubMed]
2. Basciftci, F. Investigating and comparing the two superstorms in the 23rd solar cycle. *Indian J. Phys.* **2022**, *96*, 2707–2716. [CrossRef]
3. Shi, Q.Q.; Shen, X.C.; Tian, A.M.; Degeling, A.W.; Zong, Q.; Fu, S.Y.; Pu, Z.Y.; Zhao, H.Y.; Zhang, H.; Yao, S.T. Magnetosphere response to solar wind dynamic pressure change: Vortices, ULF waves, and aurorae. In *Dayside Magnetosphere Interactions*; John Wiley and Sons: Hoboken, NJ, USA, 2020; pp. 77–97.
4. Fogg, A.R.; Jackman, C.M.; Coco, I.; Douglas Rooney, L.; Weigt, D.M.; Lester, M. Why are some solar wind pressure pulses followed by geomagnetic storms? *J. Geophys. Res. Space Phys.* **2023**, *128*, e2022JA031259. [CrossRef]
5. Bézier, P.E. *Numerical Control—Mathematics and Applications*; Forrest, A.R.; Pankhurst, A.F., Translators; John Wiley and Sons: Hoboken, NJ, USA, 1972.
6. Prautzsch, H.; Boehm, W.; Paluszny, M. *Bézier and B-Spline Techniques*; Springer: Berlin/Heidelberg, Germany, 2002.
7. Salomon, D. *Curves and Surfaces for Computer Graphics*; Springer: New York, NY, USA, 2006.
8. Erkan, E. Öklid Düzleminde ve Öklid Uzayında Bézier Eğrileri. Ph.D. Thesis, Institute of Science, Yildiz Technical University, Istanbul, Turkey, 2019. (In Turkish)

9. Eroglu, E.; Tretyakov, O.A. The Bézier curve and neural network model of the time-domain transient signals. *Comput. Phys. Commun.* **2024**, *301*, 109211. [CrossRef]
10. Eroglu, E. Bézier cubics' agreement with the neural network of the TEC map. *Soft Comput.* **2024**, *28*, 10835–10852. [CrossRef]
11. Eroglu, E.; Koksal, M.E. Bézier cubics and neural network agreement along a moderate geomagnetic storm. *Discret. Dyn. Nat. Soc.* **2024**, *2024*, 3559969. [CrossRef]
12. Soyfidan, T. Kuaterniyonik Involute-Evolut Eğri Çiftleri. Master's Thesis, Institute of Science, Sakarya University, Sakarya, Turkey, 2011. (In Turkish)
13. Sabuncuoğlu, A. *Sabuncuoglu A: Diferansiyel Geometri*, 5th ed.; Nobel Akademik Yayıncılık: Ankara, Turkey, 2016. (In Turkish)
14. Eyelade, A.V.; Stepanova, M.; Espinoza, C.M.; Antonova, E.E.; Kirpichev, I.P. The response of the Earth magnetosphere to changes in the solar wind dynamic pressure: 1. Plasma and magnetic pressures. *J. Geophys. Res. Space Phys.* **2024**, *129*, e2023JA031948. [CrossRef]
15. Vidal-Luengo, S.E.; Moldwin, M.B. Global magnetosphere response to solar wind dynamic pressure pulses during northward IMF using the heliophysics system observatory. *J. Geophys. Res. Space Phys.* **2021**, *126*, e2020JA028587. [CrossRef]
16. King, J.H.; Papitashvili, N.E. Solar wind spatial scales in and comparisons of hourly Wind and ACE plasma and magnetic field data. *J. Geophys. Res. Space Phys.* **2005**, *110*, A02104. [CrossRef]
17. Farouki, R.T. The Bernstein polynomial basis: A centennial retrospective. *Comput. Aided Geom. Des.* **2012**, *29*, 379–419. [CrossRef]
18. Huber, P.J.; Ronchetti, E.M. *Robust Statistics*; John Wiley and Sons: Hoboken, NJ, USA, 2011.
19. Cover, T.; Hart, P. Nearest neighbor pattern classification. *IEEE Trans. Inf. Theory* **1967**, *13*, 21–27. [CrossRef]
20. Jolliffe, I.T.; Cadima, J. Principal component analysis: A review and recent developments. *Philos. Trans. Ser. A Math. Phys. Eng. Sci.* **2016**, *374*, 20150202. [CrossRef] [PubMed]

Disclaimer/Publisher's Note: The statements, opinions and data contained in all publications are solely those of the individual author(s) and contributor(s) and not of MDPI and/or the editor(s). MDPI and/or the editor(s) disclaim responsibility for any injury to people or property resulting from any ideas, methods, instructions or products referred to in the content.